Flux-Weakening Controller Design of Dual Three-Phase PMSM Drive System With Copper Loss Minimization

Senyi Liu, *Member, IEEE*, Zaixin Song, *Member, IEEE*, Yuxin Liu, *Student Member, IEEE*,
Yong Chen, *Student Member, IEEE*, and Chunhua Liu, *Senior Member, IEEE*

***Abstract*—The performance of flux-weakening controllers in the multiphase permanent magnets (PM) machines depends on the accurate fundamental voltage limit derivation, and the minimal copper loss design in the flux-weakening operation region has not been well discussed. In this article, the accurate fundamental voltage limit with considering harmonic current suppression is derived at first. Then, two control concepts are addressed, and the corresponding flux-weakening control strategies are designed with the gradient descent method. In the first control strategy, both the fundamental and harmonic voltage vectors are feasible, resulting in the larger amplitude of the phase currents. The second control strategy obtains higher bus voltage utilization by an additional transition stage. At the same time, the harmonic currents cannot be further suppressed in the flux-weakening operation region. Third, the copper loss per electrical cycle is calculated, and a switching scheme is designed to obtain lower copper loss in the flux-weakening operation region. Finally, both strategies are successfully implemented in a dual three-phase PMSM. Moreover, the proposed switching scheme obtains minimal copper loss in the whole flux-weakening operation region.**

***Index Terms*—Copper loss, flux weakening control, multiphase machine, permanent magnet synchronous machine (PMSM).**

NOMENCLATURE

$F*$	Voltage or current components in the $*$-axis.
θ_e	Electrical rotor angle [rad].
R_s	Stator resistance [Ω].
L_d, L_q	Stator inductance (d, q axis, resp.) [mH].
L_{xy}	Leakage self-inductance in the xy subspace [mH].
Ψ_f	Permanent magnets (PM) flux linkage [Wb].
ω_e	Electrical rotor speed [rad/s].
u_d, u_q, u_x, u_y	Stator voltage (d, q, x, y axis, resp.) [V].
i_d, i_q, i_x, i_y	Stator current (d, q, x, y axis, resp.) [A].
e_x, e_y	Inner voltage source (x, y axis, resp.) [V].
V_{dc}	Bus voltage [V].
n_p	Number of pole pairs.
$v_{①}$–$v_{⑥}$	Candidate voltage vectors in modulation methods.
$d_{①}$–$d_{⑥}$	Duty cycle of candidate voltage vectors.
$u_{s\|*}^{\text{ref}}$	Reference voltage in the $*$-axis [V].
χ, γ	Transform angle [deg].
$V_{L*\|**}$	Voltage vector amplitude of $L*$ group in $**$ subspace.
η	Learning rate.
$V_{\max\|\alpha\beta}^{1}$	Fundamental voltage limit considering the harmonic current control [V].
$V_{\max\|\alpha\beta}^{2}$	Physical voltage limit [V].
$V_{\alpha\beta}^{\text{ref}}$	Amplitude of reference fundamental voltage vector [V].
V_m^*	Reference voltage limit [V].
$d_{\bar{x}}$, $d_{\bar{y}}$	Duty cycles of reference voltage vectors in $\bar{x}$ and $\bar{y}$ axes, respectively.

I. INTRODUCTION

DUAL three-phase permanent magnet synchronous machines (DTP-PMSMs) have better fault-tolerant capability [1], lower torque ripples, and higher torque density [2]. These key advantages can promote the application of DTP-PMSMs for propulsion, such as electrical ships [3] and electric vehicles [4].

The operation of PMSMs above the rated speed is necessary for the propulsion and the servo application [5]. The controller applied in this region is called flux-weakening (FW) control. The negative currents in the d-axis will reduce the active flux and satisfy the bus voltage limit [6].

The FW controllers in the three-phase PMSM utilize the proportional-integral (PI) to adjust the d-axis currents when the voltage commands exceed the inverter limit [7]. The closed-loop control methods do not require additional parameters, and the steady-state performance is acceptable [8]. However, tuning the additional PI controllers and the slow dynamic performance are two main disadvantages of these methods [9]. The feedforward

Manuscript received 21 May 2022; revised 27 August 2022; accepted 17 October 2022. Date of publication 21 October 2022; date of current version 18 November 2022. This work was supported in part by the grant under Project SGDX2019081623101559 of Shenzhen–Hong Kong Innovation Circle Category C Project from the Science Technology and Innovation Committee of Shenzhen Municipality, China, in part by the grant under Project ITP/027/19AP from the Innovation and Technology Commission, Hong Kong, in part by the RGC Research Fellow Scheme (RGC Ref. No.: RFS2223-1S05) from Research Grants Council, Hong Kong SAR, and in part by the Collaborative Research Fund from Research Grants Council under CRF Project C1052-21GF, Hong Kong SAR. Recommended for publication by Associate Editor I. Slama-Belkhodja. *(Corresponding author: Chunhua Liu.)*

The authors are with the School of Energy and Environment, City University of Hong Kong, Hong Kong (e-mail: senyiliu2-c@my.cityu.edu.hk; zaixin.song@cityu.edu.hk; yuxin.liu@my.cityu.edu.hk; yong.chen@my.cityu.edu.hk; chunliu@cityu.edu.hk).

Color versions of one or more figures in this article are available at https://doi.org/10.1109/TPEL.2022.3216513.

Digital Object Identifier 10.1109/TPEL.2022.3216513

controllers are alternatives to the closed-loop controllers, where the reference d-axis currents are derived from the mathematical model [10]. The fast dynamic performance is the main advantage of feedforward controllers, whereas the parameter dependence and lack of resistive voltage drop compensation will affect the steady-state performance [11]. Some hybrid methods are discussed to improve the whole speed performance of FW controllers [12], [13].

However, the harmonic current subspace is the main problem in the extension of the conventional FW controllers from the three-phase PMSM to DTP-PMSM. If the harmonic currents are suppressed, the linear fundamental voltage limit cannot reach the ideal inverter limit. For instance, the bus utilization of virtual vector-based controllers is about 7.2% lower than the ideal inverter limit [14]. Moreover, the existing FW control strategy utilizes a lower voltage limitation as the reference fundamental voltage limitation [15]. In contrast, the controllers without the active harmonic currents suppression can obtain the highest bus voltage utilization (BVU) [16], [17]. However, these controllers cause large harmonic currents even when DTP-PMSM does not operate in the FW region.

Some literature has analyzed the BVU in ac machines with additional harmonic subspaces. For instance, Zhao and Lipo [18] provide a BVU analysis of the multiphase machines under carrier-based pulsewidth modulation (PWM) modulation. In [19], the current controller for open-winding PMSM is discussed where the voltage limit is set by the zero-sequence current controller. A similar fundamental voltage limit discussion can be observed in [20] and [21]. However, the fundamental voltage limits analyzed in these papers are offline constant values. In practice, the fundamental voltage limit will be affected by the harmonic current suppression (HCS) controller and is a time-varying value that varies with operating conditions [22]. Moreover, existing papers have never discussed whether the fundamental voltage limits obtained from different modulation methods are the same.

In addition to the fundamental voltage limit analysis, there is also a problem in the FW controller design for the multiphase PMSMs. Naturally, multiphase PMSMs will have two different fundamental voltage limits. The first limit is the fundamental voltage limit with the active harmonic current control, which is much lower than the inverter limit. Moreover, this fundamental voltage limit changes with the required harmonic voltage vectors [22]. The second limit is the inverter limit, which is the physical limit. The harmonic currents cannot be controlled if the fundamental voltage amplitude approaches this limit. Thus, two different controller design concepts exist in the FW operation region.

First, the fundamental and harmonic currents will be controlled under the FW operation region. In this case, the fundamental voltage limit is less than or equal to the first voltage limit, which results in an increasing FW d-axis current. Existing literature about the FW control scheme in multiphase PMSMs mainly focuses on this control concept [15], [20]. In general, these controllers' dc-link utilization and maximum speed cannot reach the ideal performance of multiphase motors.

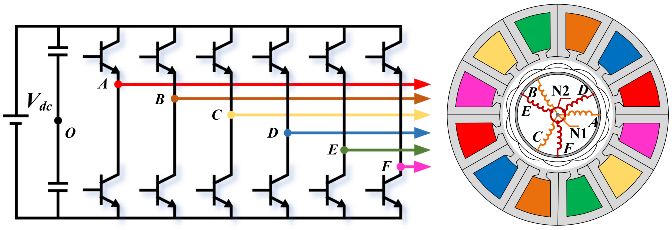

Fig. 1. Structure of DTP-PMSM drive system.

In the second control concept, the priority of the fundamental current is higher than the harmonic current control. When the fundamental voltage amplitude exceeds the first voltage limit, the controller will gradually give up HCS to obtain higher voltage utilization. Thus, the FW d-axis current is lower. While considering the existence of harmonic currents in the FW operation region, the prior copper losses calculation between these two control concepts will be discussed.

Moreover, the minimal copper loss can be obtained in the whole speed range with the prior copper losses calculation. The switching scheme between these two control concepts will be designed according to the prior copper loss calculation.

This article will discuss two voltage limits of DTP-PMSM in Section IV. Then, based on these two voltage limits, two control strategies based on two control concepts are designed in Section V. The first control strategy utilizes the first voltage limitation as the limit. The second control strategy develops an adaptive harmonic voltage vector compensation method when the amplitude of the fundamental voltage vector exceeds the first voltage limit and is less than the second voltage limit. Moreover, both control strategies utilize a novel gradient descent method to online solve the accurate FW d-axis current reference. The prior copper loss calculation and corresponding switching scheme are discussed in Section VI. Finally, the experimental results assess both controllers with the copper losses and the minimal copper losses of the switching scheme.

II. DTP-PMSM DRIVE SYSTEM

In this section, the mathematical models of DTP-PMSM are introduced. DTP-PMSM is driven by six half-bridges, as shown in Fig. 1. These half-bridges provide phase currents with shifted electrical degrees.

The voltage models of DTP-PMSM are established in the fundamental subspace ($\alpha\beta$ subspace) and harmonic subspace (xy subspace), as shown in [21]. First, the voltage and current components are transferred from phase to $\alpha\beta$ and xy subspaces

$$\begin{bmatrix} F_\alpha \\ F_\beta \\ F_x \\ F_y \end{bmatrix} = \frac{1}{3} \begin{bmatrix} 1 & -\frac{1}{2} & -\frac{1}{2} & \frac{\sqrt{3}}{2} & -\frac{\sqrt{3}}{2} & 0 \\ 0 & \frac{\sqrt{3}}{2} & -\frac{\sqrt{3}}{2} & \frac{1}{2} & \frac{1}{2} & -1 \\ 1 & -\frac{1}{2} & -\frac{1}{2} & -\frac{\sqrt{3}}{2} & -\frac{\sqrt{3}}{2} & 0 \\ 0 & -\frac{\sqrt{3}}{2} & \frac{\sqrt{3}}{2} & \frac{1}{2} & \frac{1}{2} & -1 \end{bmatrix} \begin{bmatrix} F_A \\ F_B \\ F_C \\ F_D \\ F_E \\ F_F \end{bmatrix}. \tag{1}$$

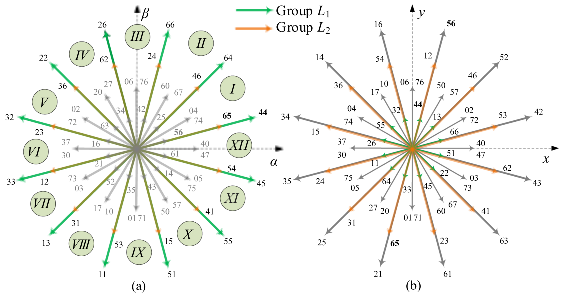

Fig. 2. Distribution of voltage vectors. (a) $\alpha\beta$ subspace. (b) *xy* subspace.

TABLE I
VOLTAGE VECTOR AMPLITUDES OF GROUPS L_1 AND L_2

Group	$V_{\alpha\beta}$	V_x	Switching States
L_1	$0.644V_{dc}$	$0.173V_{dc}$	$v_{45}, v_{44}, v_{64}, v_{66}, v_{26}, v_{22}, v_{32}, v_{33}, v_{13}, v_{11}, v_{51}, v_{55}$
L_2	$0.471V_{dc}$	$0.471V_{dc}$	$v_{54}, v_{65}, v_{46}, v_{24}, v_{62}, v_{36}, v_{23}, v_{12}, v_{31}, v_{53}, v_{15}, v_{41}$

Then, the components are transferred from the $\alpha\beta$ subspace to the *dq* synchronous reference frame, as shown in (2)

$$\begin{bmatrix} F_d \\ F_q \end{bmatrix} = \begin{bmatrix} \cos\theta_e & \sin\theta_e \\ -\sin\theta_e & \cos\theta_e \end{bmatrix} \begin{bmatrix} F_\alpha \\ F_\beta \end{bmatrix}. \tag{2}$$

The voltage models in the *dq* and *xy* subspaces are

$$\begin{bmatrix} u_d \\ u_q \end{bmatrix} = \begin{bmatrix} R_s & -\omega_e L_q \\ \omega_e L_d & R_s \end{bmatrix} \begin{bmatrix} i_d \\ i_q \end{bmatrix} + \begin{bmatrix} L_d & 0 \\ 0 & L_q \end{bmatrix} \frac{d}{dt} \begin{bmatrix} i_d \\ i_q \end{bmatrix} + \begin{bmatrix} 0 \\ \omega_e \psi_f \end{bmatrix}$$
$$\begin{bmatrix} u_x \\ u_y \end{bmatrix} = \begin{bmatrix} R_s & 0 \\ 0 & R_s \end{bmatrix} \begin{bmatrix} i_x \\ i_y \end{bmatrix} + \begin{bmatrix} L_{xy} & 0 \\ 0 & L_{xy} \end{bmatrix} \frac{d}{dt} \begin{bmatrix} i_x \\ i_y \end{bmatrix} + \begin{bmatrix} e_x \\ e_y \end{bmatrix}. \tag{3}$$

The inner voltage sources e_x and e_y include the high-order back electromotive force (EMF) components and the harmonic disturbance voltage caused by the inverter nonlinearity.

The electromagnetic torque equation is

$$T_e = 3n_p\left(\psi_f i_q + (L_d - L_q)\, i_q i_d\right). \tag{4}$$

Finally, the distribution of voltage vectors of DTP-PMSM is shown in Fig. 2. DTP-PMSM has 2^6 (64) switching states with the six half-bridges inverters. There are 48 active voltage vectors regardless of the repeated positions. These voltage vectors are classified into four groups (L_1, L_2, L_3, L_4). These groups are arranged from large to small according to their amplitudes in the $\alpha\beta$ subspace. In this article, voltage vectors in groups L_1 and L_2 are utilized and colored green and orange, respectively. Moreover, these voltage vectors split out 12 sections (I, II, III, …) in the $\alpha\beta$ subspace, as shown in Fig. 2. The voltage vector amplitudes of group L_1 and L_2 in the $\alpha\beta$ and *xy* subspaces are shown in Table I.

III. CONVENTIONAL FW CONTROL SCHEME

The existing FW control is discussed [15]. First, the outer speed loop gives the *q*-axis current reference, and the *d*-axis current reference is provided by the outer FW PI controller. If the amplitude of fundamental voltage vectors exceeds the reference V_m^*, the FW PI controller regulates the reference *d*-axis current.

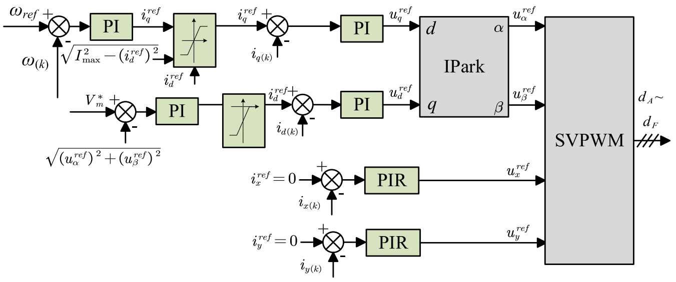

Fig. 3. Control diagram of the conventional FW control scheme.

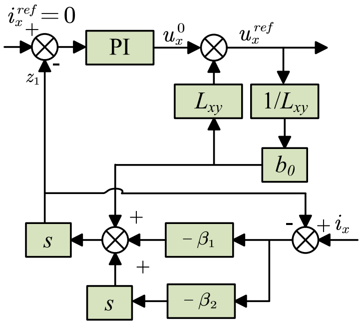

Fig. 4. Control diagram of harmonic currents controller with ESO.

Second, the reference currents in the *dq* subspaces are controlled by PI controllers, and the harmonic currents in the *xy* subspace are controlled by proportion, integration and resonantance (PIR) controllers. Finally, modified space vector PWM (SVPWM) [18] is utilized to generate the duty cycle of six half-bridges.

There are two problems in this existing FW controller. The first problem is the harmonic currents controllers, where PIR is utilized to generate the voltage command. In [22], the extended state observer (ESO) has been used to replace the PIR controllers. The mechanism is that the varying e_x and e_y [23] will affect the performance of conventional PIR controllers. ESO will compensate for the disturbance caused by the inner voltage source and inverter nonlinearity. Thus, PIR controllers in Fig. 3 are modified with PI controller with ESO, as shown in Fig. 4 [22].

The second problem is about the reference voltage limit V_m^*. In [15], the expression of voltage limit is

$$V_m^* = V_{dc}/\sqrt{3} - \Delta V \tag{5}$$

where ΔV is the reserved voltage margin for the suppression of harmonic currents. In [15], the value is set manually.

Intuitively, the tuning of ΔV is essential in the conventional FW control scheme. If ΔV is too large, the *d*-axis currents reference cannot converge to the optimum value. If ΔV is too small, the whole FW control scheme may not work correctly.

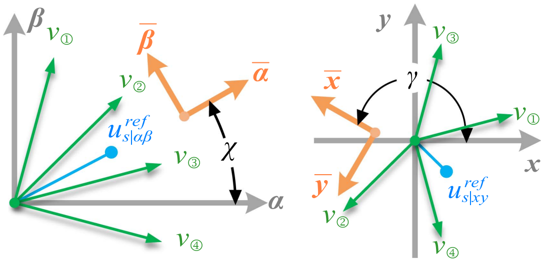

Fig. 5. Distribution of voltage vectors in the first modulation method.

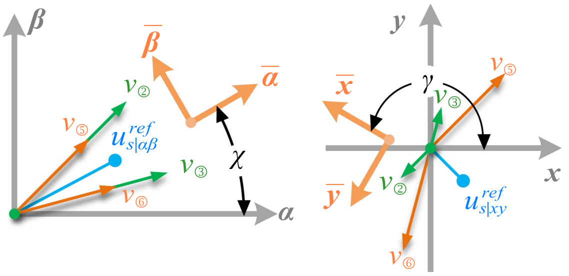

Fig. 6. Distribution of voltage vectors in the second modulation method.

IV. ACCURATE EXPRESSION OF TWO VOLTAGE LIMITS

As aforementioned, there are two voltage limits in the DTP-PMSM drive system derived here.

Both the fundamental currents and the harmonic currents are controlled in DTP-PMSM. The first fundamental voltage limit $V^1_{\max|\alpha\beta}$ is affected by the voltage components in the harmonic subspace. There are two general modulation methods in dual three-phase PMSM. The first modulation method [18] includes four voltage vectors in group L_1, and the zero-voltage vector, as given in Fig. 5. The second modulation method [24] contains two voltage vectors in group L_1, two voltage vectors in group L_2, and the zero-voltage vector, as given in Fig. 6.

There are four nonzero candidate voltage vectors and one zero voltage vector in the first and second modulation methods. In the first modulation method, $v_{\textcircled{1}}$, $v_{\textcircled{2}}$, $v_{\textcircled{3}}$, and $v_{\textcircled{4}}$ are the four candidate voltage vectors. $v_{\textcircled{2}}$ and $v_{\textcircled{3}}$ are two voltage vectors in group L_1 closest to the reference voltage vector $u^{\text{ref}}_{s|\alpha\beta}$. $v_{\textcircled{1}}$ is the voltage vector in group L_1 closest to $v_{\textcircled{2}}$, and $v_{\textcircled{4}}$ is the voltage vector in group L_1 closest to $v_{\textcircled{3}}$. Then, in the second modulation method, four candidate voltage vectors include $v_{\textcircled{2}}$, $v_{\textcircled{3}}$, $v_{\textcircled{5}}$, and $v_{\textcircled{6}}$, where $v_{\textcircled{5}}$ and $v_{\textcircled{6}}$ are two voltage vectors in group L_2 closest to the reference voltage vector $u^{\text{ref}}_{s|\alpha\beta}$.

Intuitively, two different modulation methods will cause two different $V^1_{\max|\alpha\beta}$. First, the reference voltage vectors in the $\alpha\beta$ subspace and the xy subspace are transferred into the $\bar{\alpha}\bar{\beta}$ subspace and the $\bar{x}\bar{y}$ subspace, where the directions of $\bar{\alpha}$ and $\bar{x}$ axes are always in the middle of voltage $v_{\textcircled{2}}$ and $v_{\textcircled{3}}$. The transformation matrix is expressed as

$$\begin{bmatrix} u^{\text{ref}}_{s|\bar{\alpha}} \\ u^{\text{ref}}_{s|\bar{\beta}} \end{bmatrix} = \begin{bmatrix} \cos\chi & -\sin\chi \\ \sin\chi & \cos\chi \end{bmatrix} \begin{bmatrix} u^{\text{ref}}_{s|\alpha} \\ u^{\text{ref}}_{s|\beta} \end{bmatrix} \tag{6}$$

TABLE II
MAPPING RELATIONSHIP BETWEEN SECTION AND TRANSFORMATION ANGLE

Section	*I*	*II*	*III*	*IV*	*V*	*VI*
χ (deg)	30	60	90	120	150	180
γ (deg)	150	120	90	240	30	180
Section	*VII*	*VIII*	*IX*	*X*	*XI*	*XII*
χ (deg)	210	240	270	300	330	0
γ (deg)	330	120	270	60	210	0

$$\begin{bmatrix} u^{\text{ref}}_{s|\bar{x}} \\ u^{\text{ref}}_{s|\bar{y}} \end{bmatrix} = \begin{bmatrix} \cos\gamma & -\sin\gamma \\ \sin\gamma & \cos\gamma \end{bmatrix} \begin{bmatrix} u^{\text{ref}}_{s|x} \\ u^{\text{ref}}_{s|y} \end{bmatrix} \tag{7}$$

where transformation angles χ and γ in different section are shown in Table II.

Define j equals $\pi/4$, k equals $\pi/6$, and l equals $\pi/12$, and the duty cycles of the nonzero candidate voltage vectors ($v_{\textcircled{1}}$–$v_{\textcircled{6}}$) are defined as $d_{\textcircled{1}}$, $d_{\textcircled{2}}$, $d_{\textcircled{3}}$, $d_{\textcircled{4}}$, $d_{\textcircled{5}}$, and $d_{\textcircled{6}}$. Then, the relationship between the reference voltage vector and the duty cycles in the first modulation pattern is

$$\begin{cases} u^{\text{ref}}_{s|\bar{\alpha}} = \left[(d_{\textcircled{1}}+d_{\textcircled{4}})\cos j + (d_{\textcircled{2}}+d_{\textcircled{3}})\cos l\right] V_{L1|\alpha\beta} \\ u^{\text{ref}}_{s|\bar{\beta}} = \left[(d_{\textcircled{1}}-d_{\textcircled{4}})\sin j + (d_{\textcircled{2}}-d_{\textcircled{3}})\sin l\right] V_{L1|\alpha\beta} \\ u^{\text{ref}}_{s|\bar{x}} = \left[-(d_{\textcircled{1}}+d_{\textcircled{4}})\sin k + (d_{\textcircled{2}}+d_{\textcircled{3}})\cos l\right] V_{L1|xy} \\ u^{\text{ref}}_{s|\bar{y}} = \left[-(d_{\textcircled{1}}-d_{\textcircled{4}})\cos k + (d_{\textcircled{2}}-d_{\textcircled{3}})\sin l\right] V_{L1|xy} \end{cases}. \tag{8}$$

The relationship between the reference voltage vector and the duty cycles in the second modulation pattern is

$$\begin{cases} u^{\text{ref}}_{s|\bar{\alpha}} = (d_{\textcircled{5}}+d_{\textcircled{6}})\cos l V_{L2|\alpha\beta} + (d_{\textcircled{2}}+d_{\textcircled{3}})\cos l V_{L1|\alpha\beta} \\ u^{\text{ref}}_{s|\bar{\beta}} = (d_{\textcircled{5}}-d_{\textcircled{6}})\sin l V_{L2|\alpha\beta} + (d_{\textcircled{2}}-d_{\textcircled{3}})\sin l V_{L1|\alpha\beta} \\ u^{\text{ref}}_{s|\bar{x}} = -(d_{\textcircled{5}}+d_{\textcircled{6}})\cos l V_{L2|xy} + (d_{\textcircled{2}}+d_{\textcircled{3}})\cos l V_{L1|xy} \\ u^{\text{ref}}_{s|\bar{y}} = -(d_{\textcircled{5}}-d_{\textcircled{6}})\sin l V_{L2|xy} + (d_{\textcircled{2}}-d_{\textcircled{3}})\sin l V_{L1|xy} \end{cases}. \tag{9}$$

Solving the fundamental voltage limit is converted into solving the extreme value. In the first modulation method, there is

$$\min_{d_{\textcircled{1}}, d_{\textcircled{2}}, d_{\textcircled{3}}, d_{\textcircled{4}}} \quad f_1 = \left(u^{\text{ref}}_{s|\bar{\alpha}}\right)^2 + \left(u^{\text{ref}}_{s|\bar{\beta}}\right)^2 \tag{10}$$

subject to

$$d_{\textcircled{1}} + d_{\textcircled{2}} + d_{\textcircled{3}} + d_{\textcircled{4}} = 1, d_{\textcircled{1}}, d_{\textcircled{2}}, d_{\textcircled{3}}, d_{\textcircled{4}} \in [0, 1].$$

To simplify the expression of the equation, the fractions and trigonometric functions are expressed to second decimal places. $d_{\textcircled{2}}$, $d_{\textcircled{3}}$, and $d_{\textcircled{4}}$ can be described as the function of $d_{\textcircled{1}}$ as

$$\begin{cases} d_{\textcircled{2}} = -0.93 + 3.35 d_{\textcircled{1}} + 0.26 d_{\bar{x}} + 0.33 d_{\bar{y}} \\ d_{\textcircled{3}} = 1.27 - 3.35 d_{\textcircled{1}} - 0.14 d_{\bar{x}} - 0.33 d_{\bar{y}} \\ d_{\textcircled{4}} = 0.66 - d_{\textcircled{1}} - 0.12 d_{\bar{x}} \end{cases} \tag{11}$$

where $d_{\bar{x}} = u^{\text{ref}}_{s|\bar{x}}/V_{\text{dc}}$ and $d_{\bar{y}} = u^{\text{ref}}_{s|\bar{y}}/V_{\text{dc}}$.

The derivative of (10) can be expressed as

$$\frac{d(f_1)}{d(d_{\textcircled{1}})} = \left[-6.52 + 19.80 d_{\textcircled{1}} + 6.75 d_{\bar{x}} + 6.29 d_{\bar{y}}\right] V^2_{L1|\alpha\beta}. \tag{12}$$

The necessary condition for the extreme value of (10) is (12) equals zero, and the duty cycle $d_{\textcircled{1}}$ is

$$d_{\textcircled{1}} = 0.33 - 0.34 d_{\bar{x}} - 0.32 d_{\bar{y}}. \tag{13}$$

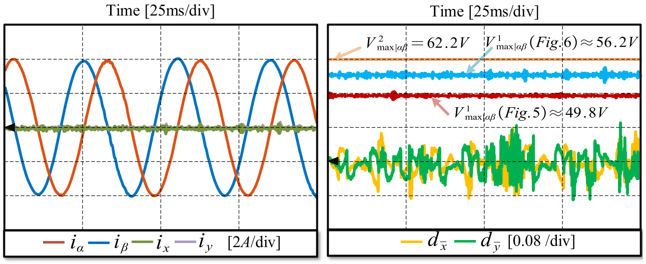

Fig. 7. Two voltage limits under 400 r/min and 10-N·m load.

Then, substitute (13) into (10), there is

$$\min_{d_{①}, d_{②}, d_{③}, d_{④}} f_1 = \left[0.26 + 0.12 d_{\bar{x}} + 0.01 d_{\bar{x}}^2\right] V_{\mathrm{dc}}^2. \quad (14)$$

In the second modulation method, there is

$$\min_{d_{②}, d_{③}, d_{⑤}, d_{⑥}} f_2 = \left(u^{\mathrm{ref}}_{s|\bar{\alpha}}\right)^2 + \left(u^{\mathrm{ref}}_{s|\bar{\beta}}\right)^2 \quad (15)$$

subject to

$$d_{②} + d_{③} + d_{⑤} + d_{⑥} = 1, d_{②}, d_{③}, d_{⑤}, d_{⑥} \in [0, 1].$$

The process is like the first modulation method, and the result is

$$\min_{d_{②}, d_{③}, d_{⑤}, d_{⑥}} f_2 = \left[0.33 + 0.31 d_{\bar{x}} + 0.07 d_{\bar{x}}^2\right] V_{\mathrm{dc}}^2. \quad (16)$$

According to the results, it can be observed that the first fundamental voltage limit $V^1_{\max|\alpha\beta}$ in the second modulation method is larger than the first modulation method. Moreover, it can be observed that only the harmonic components in the $\bar{x}$-axis affect the fundamental voltage limit. The fundamental voltage limit considering harmonic voltage vectors is expressed as

$$V^1_{\max|\alpha\beta} = \sqrt{f_2} = \sqrt{[0.33 + 0.31 d_{\bar{x}} + 0.07 d_{\bar{x}}^2]} V_{\mathrm{dc}}. \quad (17)$$

Moreover, it needs to be mentioned that the second fundamental limit occurs when only $v_{②}$ and $v_{③}$ are utilized. The second fundamental voltage limit is shown in the following equation, where the harmonic voltage vectors are uncontrolled:

$$V^2_{\max|\alpha\beta} = V_{L1|\alpha\beta} \cos l \ = \ 0.62 V_{\mathrm{dc}}. \quad (18)$$

Then, a steady-state experimental result is shown in Fig. 7 to visualize two voltage limits, where the reference speed is set as 400 r/min, and the load is placed as 10 N·m. The first limit is time-varying and lower than the second voltage limit. Moreover, the fundamental voltage limits under the two modulation methods are different, and the second modulation method obtains higher fundamental voltage utilization.

Furthermore, a simple overmodulation method is applied in this article to avoid the amplitude of the fundamental voltage vectors exceeding $V^2_{\max|\alpha\beta}$. Take the first modulation method as an example, the sum of four duty cycles is

$$d_{\mathrm{all}} = d_{①} + d_{②} + d_{③} + d_{④}. \quad (19)$$

If d_{all} is higher than one, these four duty cycles cannot be realized. Then, the normalization process is applied

$$d_i = d_i / d_{\mathrm{all}}, i = ①, ②, ③, ④. \quad (20)$$

With this overmodulation method, the fundamental voltage vectors will not exceed $V^2_{\max|\alpha\beta}$.

This section analyzes the fundamental voltage limits of two modulation methods and chooses the second modulation method in our controller. Moreover, two different fundamental voltage limits are obtained in this section. The first limit takes the harmonic voltage vectors into account, and this limit will be affected by the harmonic voltage vectors. The second limit is the physical limit of the inverter.

V. PROPOSED FW CONTROL STRATEGIES

There are two different voltage limits, according to the last section. If the fundamental voltage vectors reach the voltage limit $V^1_{\max|\alpha\beta}$, there are two choices. The first strategy, defined as strategy #1, will apply the negative *d*-axis current to ensure the feasible voltage vectors in the fundamental and harmonic subspaces. In strategy #1, there is a larger *d*-axis current because the fundamental voltage limit is lower than the physical limit $V^2_{\max|\alpha\beta}$.

The second strategy, defined as strategy #2, will modify the voltage vectors in the harmonic subspace to obtain a higher fundamental voltage limit. In strategy #2, the harmonic currents cannot be suppressed entirely, which means the total harmonic distortion (THD) will increase if the reference voltage vector approaches voltage limit $V^1_{\max|\alpha\beta}$.

Both strategies can realize the FW feature, and the main difference between them is the copper loss and maximum speed. In the first strategy, the amplitude of phase currents is higher, and the fundamental voltage limit is lower. In the second strategy, the harmonic currents cannot be well suppressed. These two control strategies will be developed in this section.

A. *Development of Strategy #1*

The *d*-axis current reference generation is discussed at first. The steady-state voltage equation in the fundamental subspace is

$$\begin{bmatrix} u_d \\ u_q \end{bmatrix} = \begin{bmatrix} R_s & -\omega_e L_q \\ \omega_e L_d & R_s \end{bmatrix} \begin{bmatrix} i_d \\ i_q \end{bmatrix} + \begin{bmatrix} 0 \\ \omega_e \psi_f \end{bmatrix}. \quad (21)$$

The amplitude of the fundamental voltage vector is

$$V^{\mathrm{ref}}_{\alpha\beta} = \sqrt{u_d^{\mathrm{ref}2} + u_q^{\mathrm{ref}2}}. \quad (22)$$

If the voltage amplitude $V^{\mathrm{ref}}_{\alpha\beta}$ is higher than the fundamental limit $V^1_{\max|\alpha\beta}$, in strategy #1, the negative *d*-axis current is applied to ensure the feasible voltage vectors in these two subspaces. Moreover, according to the last section, the varying $V^1_{\max|\alpha\beta}$ has been observed. Thus, the minimum $V^1_{\max|\alpha\beta}$ is treated as the fundamental voltage limit in strategy #1.

The voltage limit trajectory (VLT) in the *dq* current frame is derived from the following equation:

$$V^{\mathrm{ref}}_{\alpha\beta} = V^1_{\max|\alpha\beta}. \quad (23)$$

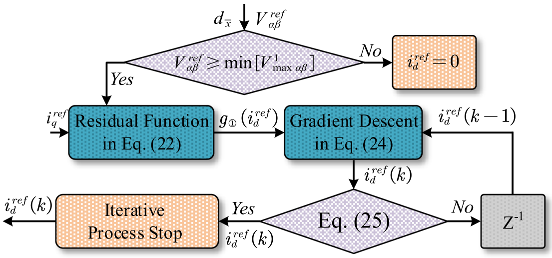

Fig. 8. Control diagram of FW strategy #1.

Then, constructing a residual function as

$$g_{①}\left(i_d^{\text{ref}}\right) = \left\{\left(V_{\alpha\beta}^{\text{ref}}\right)^2 - \left(\min\left[V_{\max|\alpha\beta}^{1}\right]\right)^2\right\}^2$$
$$= \left\{\begin{array}{l}\left(R_s i_q^{\text{ref}} + \omega_e L_d i_d^{\text{ref}} + \omega_e \psi_f\right)^2 \\ + \left(R_{si_d}^{\text{ref}} - \omega_e L_{qi_q}^{\text{ref}}\right)^2 - \left(\min\left[V_{\max|\alpha\beta}^{1}\right]\right)^2\end{array}\right\}^2 \tag{24}$$

where the voltage limit can be determined if the residual function is zero.

Thus, solving the *d*-axis current reference expression can be transformed into a problem of solving the minimum value of the residual function online. The gradient descent method is utilized, where the derivative of a residual function is

$$g'_{①}\left(i_d^{\text{ref}}\right) = 2\left\{\begin{array}{l}\left(R_s i_q^{\text{ref}} + \omega_e L_d i_d^{\text{ref}} + \omega_e \psi_f\right)^2 \\ + \left(R_s i_d^{\text{ref}} - \omega_e L_q i_q^{\text{ref}}\right)^2 - \left(\min\left[V_{\max|\alpha\beta}^{1}\right]\right)^2\end{array}\right\}$$
$$\left\{2\omega_e L_d\left(R_s i_q^{\text{ref}} + \omega_e L_d i_d^{\text{ref}} + \omega_e \psi_f\right) + 2R_s\left(R_s i_d^{\text{ref}} - \omega_e L_q i_q^{\text{ref}}\right)\right\}. \tag{25}$$

The iterative process of i_d^{ref} is expressed as

$$i_d^{\text{ref}}(k) = i_d^{\text{ref}}(k-1) + \eta g'_{①}\left(i_d^{\text{ref}}(k-1)\right). \tag{26}$$

Then, an interrupting section is applied to avoid the influence of steady-state performance. The condition is expressed as

$$\left[\left|g'_{①}\left(i_d^{\text{ref}}\right)\right| < \varepsilon\right] \wedge \left[\left|\omega - \omega_{\text{ref}}\right| < \xi\right] \tag{27}$$

which means the iterative process will stop if the derivative of (22) and the residual speed error is small enough.

The whole process of strategy #1 is shown in Fig. 8. If the reference fundamental voltage vectors exceed the minimum value of $V_{\max|\alpha\beta}^{1}$, the residual function is established according to the reference *q*-axis current and minimum value of $V_{\max|\alpha\beta}^{1}$. Then, the gradient descent method updates the reference *d*-axis current with (24). With several iterations, the reference *d*-axis current converges to VLT and derivative $g'_{(}i_d^{\text{ref}})$ will be smaller. If the derivative and the speed residual error fulfill (25), the iterative process will stop.

B. Development of Strategy #2

Compared with strategy #1, strategy #2 will modify the harmonic voltage vectors to ensure the feasible fundamental voltage vectors if the reference fundamental voltage vector exceeds the first voltage limit and be less than the second voltage limit. The whole process of strategy #2 is shown in Fig. 9, which includes two regions.

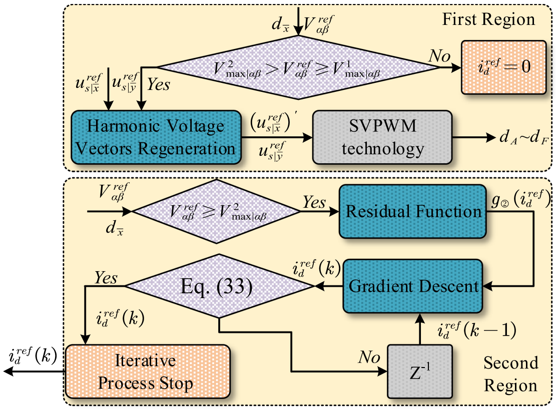

Fig. 9. Control diagram of FW strategy #2.

The harmonic voltage vectors are modified in the first region to ensure the feasible voltage vectors in the fundamental subspace. According to (17), the increasing trend of voltage limit $V_{\max|\alpha\beta}^{1}$ with $d_{\bar{x}}$ can be observed. Thus, $d_{\bar{x}}$ is modified to obtain higher bus utilization. Defined the modified $d_{\bar{x}}$ as $d'_{\bar{x}}$, the equation is expressed as

$$\left[0.33 + 0.31d'_{\bar{x}} + 0.07\left(d'_{\bar{x}}\right)^2\right] V_{\text{dc}}^2 \geqslant \left(V_{\alpha\beta}^{\text{ref}}\right)^2. \tag{28}$$

For simplification, there is

$$\left[0.33 + 0.31d'_{\bar{x}} + 0.07\left(d'_{\bar{x}}\right)^2\right] V_{\text{dc}}^2 \geqslant$$

$$\left[0.33 + 0.31d'_{\bar{x}}\right] V_{\text{dc}}^2 \geqslant \left(V_{\alpha\beta}^{\text{ref}}\right)^2. \tag{29}$$

Then, the feasibility of fundamental voltage vectors can be ensured with $d'_{\bar{x}}$

$$d'_{\bar{x}} = \left[\left(V_{\alpha\beta}^{\text{ref}}\right)^2 / V_{\text{dc}}^2 - 0.33\right] / 0.31. \tag{30}$$

With the increasing fundamental voltage vectors, $d'_{\bar{x}}$ will reach the maximum value, which can be expressed as

$$\left[0.33 + 0.31d'_{\bar{x}} + 0.07\left(d'_{\bar{x}}\right)^2\right] V_{\text{dc}}^2 = \left(V_{\max|\alpha\beta}^{2}\right)^2. \tag{31}$$

Solving (29), the maximum $d'_{\bar{x}}$ is about 0.17. In summary, the duty cycle $d_{\bar{x}}$ will be modified as $d'_{\bar{x}}$ according to the amplitude of the fundamental voltage vectors: This also means that the harmonic voltages are no longer controlled by the current controller but are determined by the amplitude of the fundamental voltage vectors in the FW region

$$d'_{\bar{x}}$$
$$= \left\{\begin{array}{l}\left[\left(V_{\alpha\beta}^{\text{ref}}\right)^2 / V_{\text{dc}}^2 - 0.33\right] / 0.31, V_{\max|\alpha\beta}^{1} \leqslant V_{\alpha\beta}^{\text{ref}} \leqslant V_{\max|\alpha\beta}^{2} \\ \qquad 0.17, V_{\alpha\beta}^{\text{ref}} > V_{\max|\alpha\beta}^{2}\end{array}\right.. \tag{32}$$

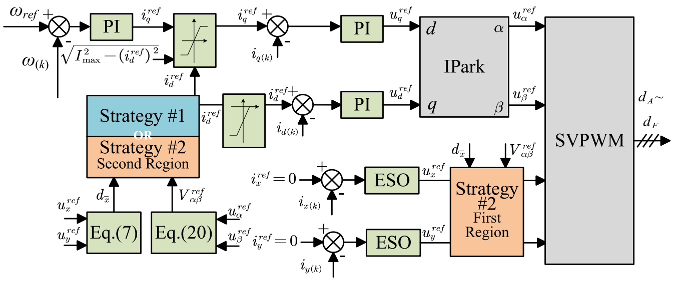

Fig. 10. Total control process.

Then, the voltage vectors in the harmonic subspace are

$$\begin{cases} u_{s|\bar{x}}^{\text{ref}} = d'_{\bar{x}} V_{\text{dc}} \\ u_{s|\bar{y}}^{\text{ref}} = u_{s|\bar{y}}^{\text{ref}} \end{cases}. \tag{33}$$

The inverse transform matrix is utilized as

$$\begin{bmatrix} u_{s|x}^{\text{ref}} \\ u_{s|y}^{\text{ref}} \end{bmatrix} = \begin{bmatrix} \cos\gamma & \sin\gamma \\ -\sin\gamma & \cos\gamma \end{bmatrix} \begin{bmatrix} u_{s|\bar{x}}^{\text{ref}} \\ u_{s|\bar{y}}^{\text{ref}} \end{bmatrix}. \tag{34}$$

Then, in the second region, the amplitude of the reference voltage vector exceeds the second voltage limit. Similarly, the residual function is expressed as

$$\begin{aligned} g_{②}\left(i_d^{\text{ref}}\right) &= \left\{ \left(V_{\alpha\beta}^{\text{ref}}\right)^2 - \left(V_{\max|\alpha\beta}^2\right)^2 \right\}^2 \\ &= \left\{ \begin{aligned} &\left(R_s i_q^{\text{ref}} + \omega_e L_d i_d^{\text{ref}} + \omega_e \psi_f\right)^2 \\ &+\left(R_s i_d^{\text{ref}} - \omega_e L_q i_q^{\text{ref}}\right)^2 - \left(V_{\max|\alpha\beta}^2\right)^2 \end{aligned} \right\}^2. \end{aligned} \tag{35}$$

The derivative of this residual function is

$$\begin{aligned} g'_{②}\left(i_d^{\text{ref}}\right) = 2 &\left\{ \begin{aligned} &\left(R_s i_q^{\text{ref}} + \omega_e L_d i_d^{\text{ref}} + \omega_e \psi_f\right)^2 \\ &+\left(R_s i_d^{\text{ref}} - \omega_e L_q i_q^{\text{ref}}\right)^2 - \left(V_{\max|\alpha\beta}^2\right)^2 \end{aligned} \right\} \\ &\left\{2\omega_e L_d \left(R_s i_q^{\text{ref}} + \omega_e L_d i_d^{\text{ref}} + \omega_e \psi_f\right) \right. \\ &\left. + 2R_s \left(R_s i_d^{\text{ref}} - \omega_e L_q i_q^{\text{ref}}\right)\right\}. \end{aligned} \tag{36}$$

The iterative process of i_d^{ref} is expressed as

$$i_d^{\text{ref}}(k) = i_d^{\text{ref}}(k-1) + \eta g'_{②}\left(i_d^{\text{ref}}(k-1)\right). \tag{37}$$

The interrupting condition is expressed as

$$\left[\left|g'_{②}\left(i_d^{\text{ref}}\right)\right| < \varepsilon\right] \wedge \left[\left|\omega - \omega_{\text{ref}}\right| < \xi\right]. \tag{38}$$

C. General Control Process and Convergence Speed

Fig. 10 provides the general control process. First, the *q*-axis current reference is also determined from the residual error of speed. Second, the *d*-axis current reference is determined by the FW strategies in Figs. 8 and 9.

Compared with the conventional FW strategies in Fig. 3, both strategies in this article require the harmonic voltage vector information to obtain the precise fundamental voltage limit. This is the reason why we utilize the ESO in [22] because the harmonic voltage vectors will affect $V_{\max|\alpha\beta}^1$.

Moreover, in strategy #2, the harmonic voltage vectors are modified to obtain higher bus utilization in the output voltage of ESO. Finally, these voltage vectors are realized with the SVPWM technology.

TABLE III
COMPARISON WITH EXISTING CONTROLLERS

Controllers	Voltage limit	HCS in MTPA	HCS in FW
[6], [25]	$0.62V_{\text{dc}}$	No	No
Strategy #2	$0.62V_{\text{dc}}$	Yes	No
[15], [26]	$0.62V_{\text{dc}}$-ΔV	Yes	Yes
Strategy #1	$V_{\max\|\alpha\beta}^1$	Yes	Yes

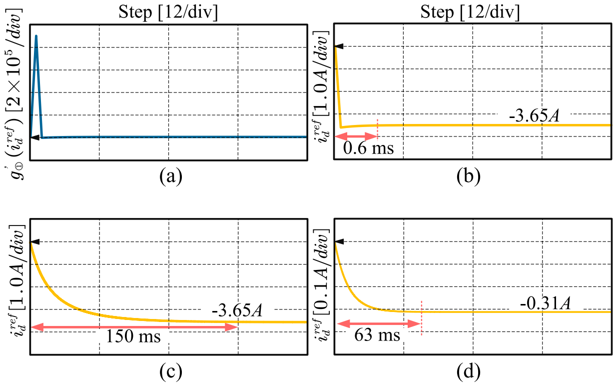

Fig. 11. Convergence speed assessment. (a) Gradient descent function under $V_{\max|\alpha\beta}^1$. (b) Reference *d*-axis current of gradient descent method. (c) Reference *d*-axis current of PI controller under $V_{\max|\alpha\beta}^1$. (d) Reference *d*-axis current of PI controller under $V_{\max|\alpha\beta}^2$.

Since the gradient descent method is utilized in this article, the convergence speed will be assessed. Take DTP-PMSM in Table III as an example; the reference value of *d*-axis current in the normal operation mode is zero. If the reference speed is set above the rated speed, and this reference speed is applied in (23), the converging speed of the gradient descent method can be observed. Similarly, the converging speed of the conventional PI-based controller can also be obtained by this method. The reference speed is 1000 r/min, and the learning rate is 1e-7 in Fig. 11(a) and (b). According to the results in Fig. 11(b), the reference value of *d*-axis current will converge to the stable value –3.65 A within six steps, where the residual ε is set as 0.01 A. The results of the PI-based controller are shown in Fig. 11(c), where the PI coefficient is

$$k_{p|FW} = 0.005, k_{i|FW} = 0.16. \tag{39}$$

According to Fig. 11(c), the reference *d*-axis current will also converge to the stable value –3.65 A. However, the conventional PI-based FW controller will consume more steps to reach this stable value. Moreover, the convergence speed of PI-based method will change according to the utilized voltage limit. In Fig. 11(d), $V_{\max|\alpha\beta}^2$ is utilized where the convergence time is about 630 steps.

In contrast, the PI-based controller will consume 150 ms in Fig. 11(c) and 63 ms in Fig. 11(d). In summary, the gradient descent method utilized in this article is dependent on the accurate parameters. Still, it can significantly reduce the convergence time of the FW current reference generation and avoid the worse dynamic performance caused by the longer convergence time in the PI-based method.

VI. MINIMAL COPPER LOSS SCHEME DESIGN

Two different FW controllers designed for DTP-PMSM have been discussed in the last section. The main difference is the fundamental voltage limit utilized in the FW controller. In strategy #1, the harmonic currents are suppressed in the FW operation region, and the fundamental voltage utilization is lower than the physical limit. Thus, the amplitude of d-axis current will be larger in the FW operation region. Strategy #2 has a transition stage before the FW operation region. The fundamental voltage utilization will increase in this stage while the harmonic currents cannot be further suppressed, and the inverter will cause additional harmonic currents. We want to obtain minimal copper loss in the whole speed range. Thus, the switching between strategies #1 and #2 is necessary and will be discussed in this section.

A. Switching Scheme Design With Prior Copper Losses Calculation

The prior copper loss calculation under different strategies is discussed at first. Since the copper losses from current ripples are challenging to express in an accurate mathematical model. The copper loss caused by ripples is similar in the same DTP-PMSM drive system. The prior copper loss in this section will only include the copper loss from the fundamental currents and the harmonics currents.

First, the copper loss per electrical cycle is defined as

$$E = \int_0^{2\pi/\omega_e} R_s \left(i_A^2 + i_B^2 + i_C^2 + i_D^2 + i_E^2 + i_F^2\right) dt. \quad (40)$$

This value is a constant in the steady-state situation and is utilized to represent the copper loss of two strategies. Thus, the copper loss caused by the fundamental currents is given as

$$\begin{aligned} E_{\alpha\beta} &= R_s\left(i_d^2 + i_q^2\right) \\ &\times \int_0^{\frac{2\pi}{\omega_e}} \begin{bmatrix} \sin^2(\omega_e t) + \sin^2(\omega_e t - \pi/6) \\ +\sin^2(\omega_e t - 2\pi/3) + \sin^2(\omega_e t - 5\pi/6) \\ +\sin^2(\omega_e t - 4\pi/3) + \sin^2(\omega_e t - 3\pi/2) \end{bmatrix} dt \quad (41) \\ &= 6\pi R_s\left(i_d^2 + i_q^2\right)/\omega_e. \end{aligned}$$

Then, when the amplitude of the reference fundamental voltage vector exceeds $V^1_{\max|\alpha\beta}$, the controller will gradually give up the HCS to obtain higher BVU. In the FW operation region, the fundamental BVU can reach $V^2_{\max|\alpha\beta}$. At the same time, the harmonic currents are caused by both the harmonic voltage vectors from the inverter and the inner voltage sources. The inner voltage sources are mainly caused by the high-order back EMF

$$\begin{bmatrix} e_x \\ e_y \end{bmatrix} = \begin{bmatrix} -5\omega_e\psi_{5f}\sin(6\theta_e) - 7\omega_e\psi_{7f}\sin(6\theta_e) \\ 5\omega_e\psi_{5f}\cos(6\theta_e) - 7\omega_e\psi_{7f}\cos(6\theta_e) \end{bmatrix}. \quad (42)$$

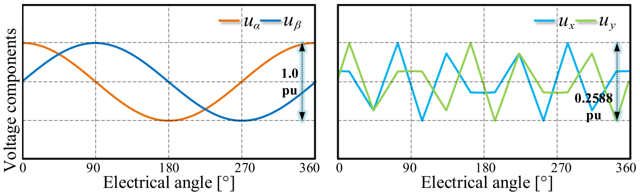

Fig. 12. Offline voltage vectors in strategy #2.

Moreover, the harmonic voltage vectors in strategy #2 caused by the inverter are shown in Fig. 12. The copper loss in strategy #2 is caused by both the fundamental and harmonic currents. It can be observed from Fig. 12 that the harmonic voltage vectors are difficult to be expressed with a precise mathematical model. Thus, the offline predictive model is applied to calculate the copper loss in the harmonic subspaces. According to (3), the discrete predictive model in the harmonic subspaces is

$$i_{x(k+1)} = \left(1 - \frac{T_{\omega e}}{L_{xy}}\right) i_{x(k)} + \frac{T_{\omega e}}{L_{xy}}\left(u_{x(k)} - e_{x(k)}\right) \quad (43)$$

where $T_{\omega e}$ is the time interval related to speed. In this article, this interval is

$$T_{\omega e} = \frac{\pi}{180\omega_e}. \quad (44)$$

The voltage vectors in Fig. 12 are sampled with 360 points per electrical period, and the sampled value is applied in (44) to calculate the predictive current. Then, the copper loss per electrical cycle caused by the harmonic currents is expressed as

$$E_{xy} = \sum_{k=1}^{359} 3R_s\left(i_{x(k)}^2 + i_{y(k)}^2\right). \quad (45)$$

The fundamental currents mainly cause the copper loss in strategy #1, and the copper loss in one electrical period is expressed as

$$E_{\text{copper}|\#1} = E_{\alpha\beta}. \quad (46)$$

In strategy #2, both the harmonic currents and fundamental currents cause copper loss, and the total copper loss per cycle is expressed as

$$E_{\text{copper}|\#2} = E_{\alpha\beta} + E_{xy}. \quad (47)$$

B. Operation Region Analysis of Both Strategies

The operation region analysis is necessary for a minimal copper loss scheme. First, the FW operation region of both strategies is shown in Fig. 13.

In strategy #1, there are only two operation regions; the blue region is the MTPA operation region ($i_d^{\text{ref}} = 0$), and the yellow region is the FW operation region. While in strategy #2, there is an additional green region that represents the MTPA operation without HCS.

Then, we will provide the characteristics of prior copper loss under the no-load condition and the 3-N·m load condition in Fig. 14. Strategy #2 is in the MTPA operation region without HCS (a green region in Fig. 13) when strategy #1 enters the FW operating region. In this situation, the additional copper loss caused by the harmonic currents is large in strategy #2, and the

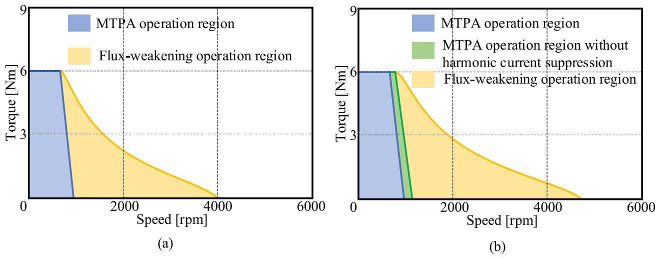

Fig. 13. Operation region of strategies #1 and #2. (a) Operation region of strategy #1. (b) Operation region of strategy #2.

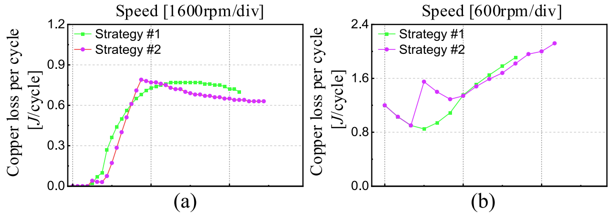

Fig. 14. Copper losses of two strategies. (a) No-load condition. (b) 3-N·m load condition.

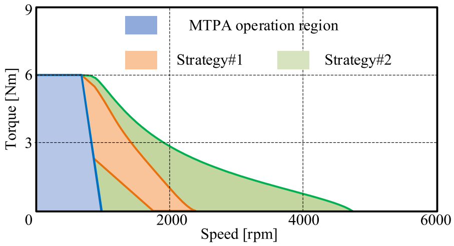

Fig. 15. Operation region with optimized copper loss.

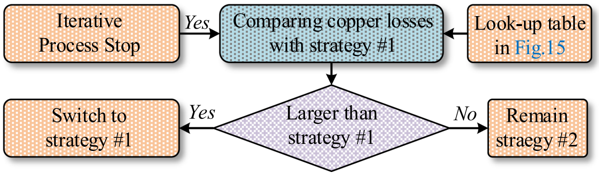

Fig. 16. Switching process between two strategies.

total copper loss of strategy #2 is larger than in strategy #1. While the copper loss caused by the harmonic currents decreases with the increasing speed. Thus, with the increasing speed, the total copper loss of strategy #2 is lower than strategy #1 because of the smaller *d*-axis currents caused by higher BVU. Moreover, the feasible operation speed of strategy #2 is also larger than strategy #1. The accuracy of the prior copper losses calculation is also assessed with the experiment where the copper losses of two strategies are tested under no-load condition and 3-N·m load condition. The copper losses measured from the experiment are a bit larger than the calculated value because of the additional copper losses caused by the current ripples. According to the experimental data, the maximum error between the experimental and calculated copper losses is about 3.2%.

Fig. 15 provides the operation region of strategies #1 and #2 under minimal copper loss design, where the blue one is the MTPA region, the orange one is the operation region of strategy #1, and the green one is the operation region of strategy #2. Finally, according to the operation region in Figs. 13 and 15, the switching scheme between two strategies can be designed. First, strategy #2 will be applied as the universal control strategy. The mechanism is that the operation region of strategy #2 is larger than strategy #1. Moreover, the copper loss of strategy #2 is lower than strategy #1 with the increasing speed. Then, the total controller will switch from strategy #2 to strategy #1, according to Fig. 15, when the iteration process of the FW controller is completed and lasts for a while. The whole process is shown in Fig. 16.

C. Comparison With Existing Methods

This section will provide the features and analysis of the proposed two strategies and existing FW controllers. Compared with the FW controllers in the conventional three-phase PMSM, there are two voltage limits in DTP-PMSM. Thus, the main difficulty in designing an FW controller for DTP-PMSM is handling these two voltage limits. There are mainly two types of FW controllers.

The first type of FW controllers will utilize the second voltage limit $V^2_{\max|\alpha\beta}$ as the reference voltage [6], [25], which is the physical voltage limit of the inverter, as shown in Fig. 7. In Table III, the features of these FW controllers are provided. The BVU of these methods is $0.62V_{\rm dc}$. However, these controllers cannot suppress the harmonic currents in the MTPA operation region. The copper losses in the non-FW operation region will be higher. In this article, strategy #2 is designed to obtain a higher BVU and avoid the additional copper losses in the MTPA region at the same time. In strategy #2, a transient section is developed to increase the BVU from $V^1_{\max|\alpha\beta}$ to $V^2_{\max|\alpha\beta}$. Then, the harmonic currents are suppressed in the MTPA region, and the BVU is $V^2_{\max|\alpha\beta}$ in the FW region.

The second type of FW controllers will utilize a lower voltage limit as the reference voltage. These controllers suppose that the harmonic currents are entirely suppressed in the whole speed range. However, the main problem in these methods is that the accurate voltage limit has not been well discussed. For instance, the voltage limit in [15] will be tuned manually with ΔV, and the dual *dq* frame is utilized in [26] to avoid the discussion of an accurate voltage limit considering HCS. In strategy #1, this lower voltage limit $V^1_{\max|\alpha\beta}$ is derived from the modulation methods, which is a parameter varying with the modulation methods and operation conditions. With this accurate voltage limit, the harmonic currents can be well suppressed in the whole speed range. According to Table III, strategy #1 can provide an accurate voltage limit and avoid the manual tuning in voltage limit. Moreover, another copper losses minimization method is discussed to further take the advantages of both strategies. With the prior copper losses calculation, the controller will switch from strategy #2 to #1 and obtain minimal copper losses in the whole speed range.

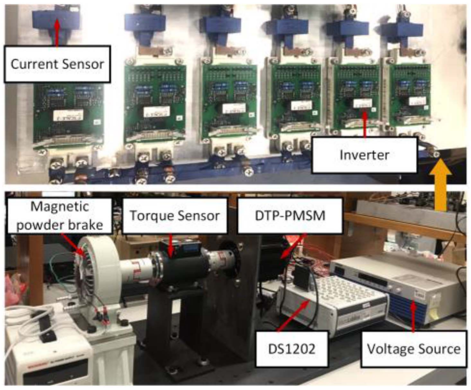

Fig. 17. Experimental platform.

TABLE IV
PARAMETER OF DTP-PMSM

Parameter	Description	Value	Parameter	Description	Value
P	Number of pole pairs	5	J(kg.m2)	Rotational inertia	0.0016
R_s(Ω)	Stator resistance	2.08	V_{DC}(V)	DC bus voltage	100
L_d(mH)	Inductance in d- axis	19.5	Speed (r/min)	Rated speed	500
L_q(mH)	Inductance in q- axis	19.5	Torque (Nm.)	Rated torque	6
L_{xy}(mH)	Leakage Inductance	5.8	Ψ_{5f}(mWb)	No-load 5th flux linkage	1.09
ψ_f(Wb)	Magnet flux linkage	0.095	Ψ_{7f}(mWb)	No-load 7th flux linkage	0.84

VII. EXPERIMENTAL RESULTS

In this section, the experiments are provided to assess the performance of the proposed two strategies and conventional FW control scheme mentioned in Section III. The experimental platform is shown in Fig. 17, where the parameter of proposed DTP-PMSM is listed in Table IV, and the control frequency is 10 kHz. The dc power supplies the bus voltage, and the control actions are performed by DS1202. The magnetic powder brake is taken as the load.

A. Performance Assessment of Strategy #1

In this section, strategy #1 and the conventional scheme in Section III are compared. The main difference between these two controllers is the reference fundamental voltage limit and the generation of reference d-axis current. Fig. 18 provides the dynamic performance of strategy #1, where the load is set as 4.5 N·m, and the reference speed is set from 200 to 1000 r/min. The system will transfer from the blue region of Fig. 13(a) to the yellow region of Fig. 13(a). The speed PI controller coefficients in this section are

$$k_p = 0.003, k_i = 0.5. \tag{48}$$

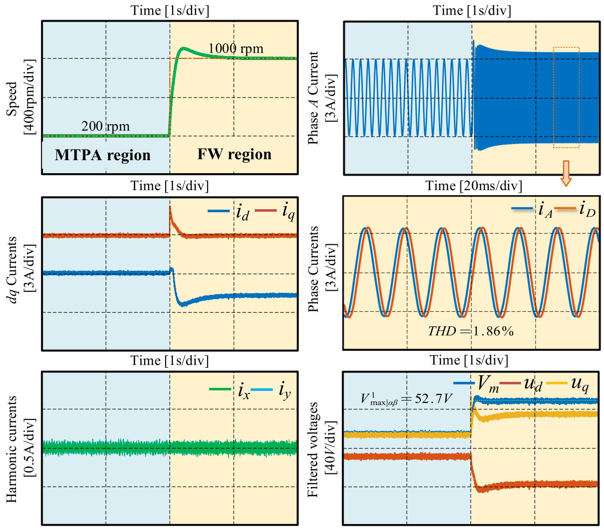

Fig. 18. Performance assessment of strategy #1.

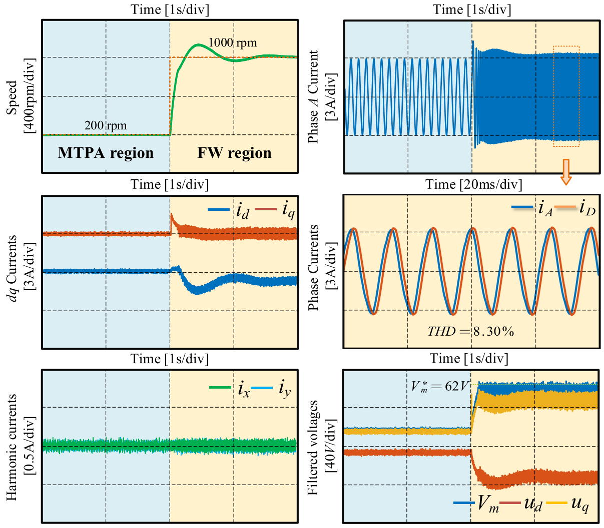

Fig. 19. Performance of conventional scheme with $V_m^* = 62$ V.

In this situation, $\min[V^1_{\max|\alpha\beta}]$ is about 52.7 V, and $V^2_{\max|\alpha\beta}$ is about 62.2 V. The fundamental voltage limit in strategy #1 is much lower than the physical limit of the inverter. The fast dynamic performance can be observed in Fig. 18. The THD in the FW region is 1.86%. With the accurate fundamental voltage limit, strategy #1 can realize both the fundamental current control and the HCS in the FW region. However, in the conventional controller without the optimized fundamental voltage limit, the performance of FW controller will be affected by the fundamental voltage limit.

For instance, if the fundamental voltage limit is larger than $V^1_{\max|\alpha\beta}$, both the fundamental voltage vectors and the harmonic voltage vectors are not feasible, which will cause distortion in the phase currents. In Fig. 19, the reference voltage limit is set as 62 V, which is higher than $V^1_{\max|\alpha\beta}$. The fundamental voltage vectors cannot reach 62 V because of the HCS. Thus, the fundamental currents distort because of the unfeasible fundamental voltage vectors. And the THD in the FW operation region is

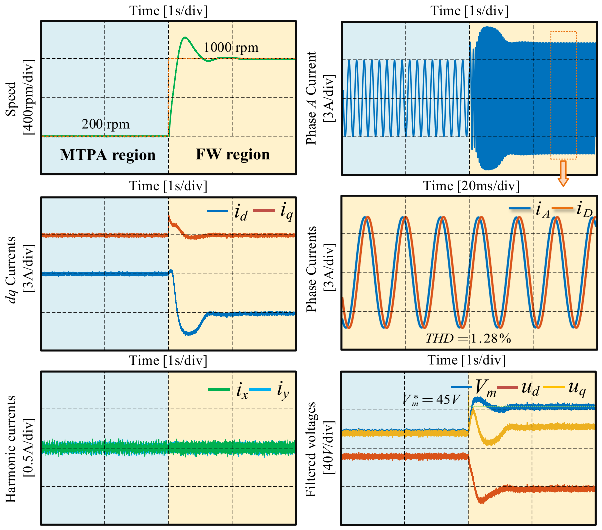

Fig. 20. Performance of conventional scheme with V_m^*=45 V.

8.30%. The total copper loss per electrical cycle is also larger than strategy #1.

In contrast, the lower fundamental voltage limit will cause an increase in phase currents. In Fig. 20, $V_{\rm m}^*$ is set as 45 V, which is lower than the optimized value 52.7 V. According to the phase current in Fig. 20, the amplitude of the phase currents in the FW operation region is much higher than the amplitude in both Figs. 18 and 19. Thus, the copper loss of this method is also larger than strategy #1.

In conclusion, the accurate $V^1_{\max|\alpha\beta}$ is the crucial factor in the FW controller design. The PI-based controller cannot realize ideal performance if $V_{\rm m}^*$ is different from $V^1_{\max|\alpha\beta}$. In contrast, strategy #1 can realize fast dynamic performance and good steady-state performance with accurate $V^1_{\max|\alpha\beta}$.

B. *Performance Assessment of Strategy #2*

The performance of strategy #2 will be discussed in this section. According to Fig. 13(b), there are three operation regions. Thus, the load is set as 3 N·m, and the reference speed is set from 200 (MTPA region) to 900 r/min (MTPA without HCS) and 1200 r/min (FW operation region).

According to Fig. 21, strategy #2 will gradually give up the HCS. Thus, the harmonic currents will cause additional copper loss and THD outside the MTPA region. In contrast, the BVU will reach 62.2 V, which is the physical limit of the inverter. Moreover, with the increasing speed, the harmonic currents caused by the inner voltage source and voltage vectors from the inverter will decrease, which is the same as in Section VI.

The calculated copper losses in Section V are also evaluated in this experiment. In Fig. 14, the copper losses of strategy #2 under 900 and 1200 r/min are 1.52 and 1.32 J/cycle, respectively. In Fig. 21, the copper losses of strategy #2 under 900 and 1200 r/min are 1.55 and 1.34 J/cycle, respectively. The maximum inaccuracy is about 2.0%, which means the prior copper losses calculation in Fig. 14 is accurate.

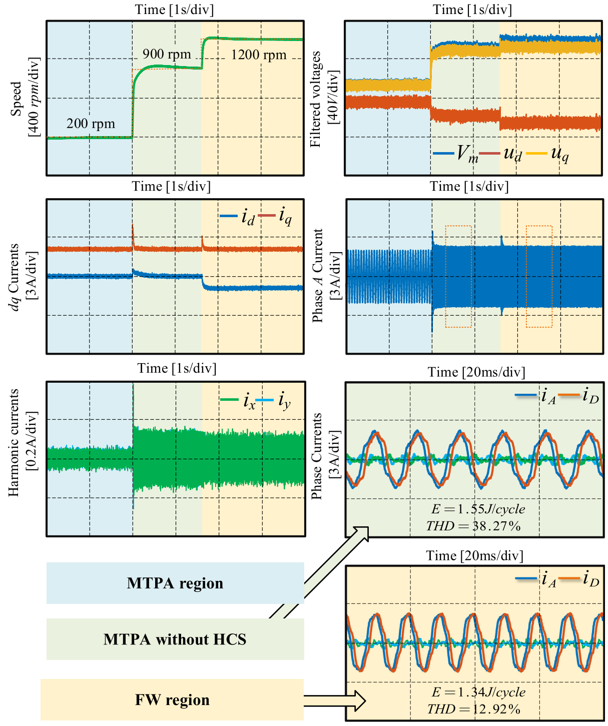

Fig. 21. Performance of strategy #2.

C. *Performance Assessment of Proposed Switching Scheme*

In this section, we will assess the switching scheme. According to Figs. 13 and 15, the operation region of strategy #2 is larger than strategy #1, and the copper loss of strategy #1 will be lower than that of strategy #2 in specific operation region. Thus, the switching scheme will always transfer from strategy #2 to strategy #1 according to the copper loss.

In Fig. 22, the system accelerates from 200 to 1100 r/min under the 3-N·m load. The switching scheme in Fig. 16 will be applied when the system is stable for 2 s. Thus, in 1100-r/min situation, strategy #2 should be transferred to strategy #1, according to Fig. 15. According to Fig. 22, the switching process from strategy #2 to strategy #1 is realized. Moreover, there is a speed fluctuation (5 r/min) in the switching process, which is caused by the voltage command varying from the PI controller.

D. *Copper Losses Assessment of Existing Controllers*

In this section, we will assess the copper losses of the existing controllers. The conventional PI-based FW controller with manually tuned voltage limit [15], the adaptative FW controller (AFC) without HCS [25], strategy #1, strategy #2, and the switching scheme are compared under the no-load condition. In this section, the non-FW operation region is colored with blue, and the FW operation region is colored with yellow.

In Fig. 23(a), the copper losses of the conventional PI-based FW controller with manually tuned voltage limit [15] and strategy #1 are provided. According to Fig. 23(a), it can be observed that the copper losses of the conventional controller vary with the manually tuned value ΔV. If ΔV is well tuned to make the voltage limit to close $\min[V^1_{\max|\alpha\beta}]$, which has been derived from

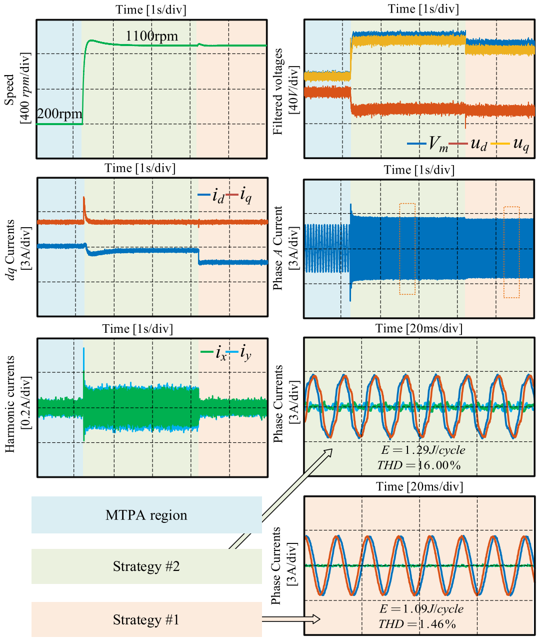

Fig. 22. Performance of switching scheme.

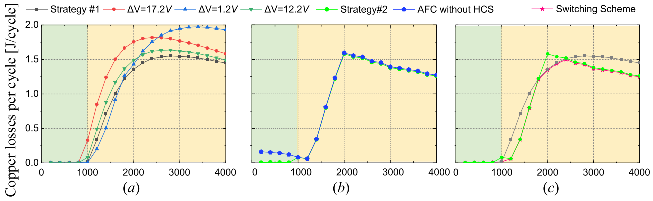

Fig. 23. Copper losses comparison of different control schemes. a) Comparison with conventional PI controller. (b) Comparison with AFC without HCS. (c) Comparision between strategy #1, #2 and switching scheme.

Section IV, the copper losses of the conventional controller will be similar to the copper losses of strategy #1. In other words, strategy #1 is an improved version of the conventional PI-based FW controller.

In Fig. 23(b), the copper losses of the adaptative FW controller without HCS [25] and strategy #2 are provided. The BVU of these two methods is 0.62 V_{dc}. While the copper losses of the adaptative FW controller without HCS in the non-FW operation region is larger than strategy #2. The mechanism is that the adaptative FW controller without HCS cannot suppress the harmonic currents in the MTPA region. In contrast, strategy #2 has developed a novel transient section to realize both the high BVU and HCS in the MTPA region. Therefore, strategy #2 is an improved version of the AFC without HCS [25].

Finally, the copper losses of strategy #1, strategy #2, and the switching scheme are shown in Fig. 23(c). According to the last two figures, both strategies #1 and #2 have lower copper losses compared to the existing FW controllers. In Fig. 23(c), the switching scheme has the lowest copper losses in the whole speed range. The mechanism is that the switching scheme can utilize the prior copper losses calculation in Section V to decide which strategy will be utilized in the steady state. Thus, the switching scheme can obtain the lowest copper losses in the whole speed range.

VIII. CONCLUSION

The harmonic currents are controlled in the conventional FW controller applied in the multiphase PMSMs. However, this control concept cannot realize a minimal copper loss in the FW operation region. This article discusses the accurate fundamental voltage limits considering the harmonic currents suppression and develops two control strategies according to this dynamic fundamental voltage limit. Then, the prior copper loss calculation and the switching scheme are applied to obtain the minimal copper loss in the whole FW operation region.

The contribution of this article includes two points.

1) The accurate fundamental voltage limit considering HCS ($V^1_{\max|\alpha\beta}$) is derived in this article. This voltage limit is lower than the maximum voltage limit $0.62V_{\mathrm{dc}}$. Moreover, this voltage limit is not a constant as assumed in the past literatures [2], [6], [25]. This limit will vary with the reference harmonic voltage vectors and modulation methods.
2) Suppressing the harmonic currents in the FW operation conditions is not the optimal choice considering about the total copper losses and maximum speed. With the increasing speed, giving up HCS to obtain higher BVU can result in lower copper losses.

REFERENCES

[1] M. Mengoni, L. Zarri, A. Tani, L. Parsa, G. Serra, and D. Casadei, “High-torque-density control of multiphase induction motor drives operating over a wide speed range,” *IEEE Trans. Ind. Electron.*, vol. 62, no. 2, pp. 814–825, Feb. 2015, doi: 10.1109/TIE.2014.2334662.

[2] E. Levi, “Multiphase electric machines for variable-speed applications,” *IEEE Trans. Ind. Electron.*, vol. 55, no. 5, pp. 1893–1909, May 2008, doi: 10.1109/TIE.2008.918488.

[3] L. Parsa and H. A. Toliyat, “Five-phase permanent magnet motor drives for ship propulsion applications,” in *Proc. IEEE Electric Ship Technol. Symp.*, 2005, pp. 371–378, doi: 10.1109/ESTS.2005.1524702.

[4] W. Li, T. W. Ching, K. T. Chau, and C. H. T. Lee, “A superconducting vernier motor for electric ship propulsion,” *IEEE Trans. Appl. Supercond.*, vol. 28, no. 3, Apr. 2018, Art. no. 5201706, doi: 10.1109/TASC.2017.2787136.

[5] W. Fan, X. Zhu, L. Quan, W. Wu, L. Xu, and Y. Liu, “Flux-weakening capability enhancement design and optimization of a controllable leakage flux multilayer barrier PM motor,” *IEEE Trans. Ind. Electron.*, vol. 68, no. 9, pp. 7814–7825, Sep. 2021, doi: 10.1109/TIE.2020.3016253.

[6] S. Liu and C. Liu, “Flux weakening control for dual three-phase PMSM,” in *Proc. Asia-Pacific Magn. Recording Conf.*, 2018, pp. 1–2, doi: 10.1109/APMRC.2018.8601058.

[7] L. Harnefors, K. Pietilainen, and L. Gertmar, “Torque-maximizing field-weakening control: Design, analysis, and parameter selection,” *IEEE Trans. Ind. Electron.*, vol. 48, no. 1, pp. 161–168, Feb. 2001.

[8] J. Su, R. Gao, and I. Husain, “Model predictive control based field-weakening strategy for traction EV used induction motor,” *IEEE Trans. Ind. Appl.*, vol. 54, no. 3, pp. 2295–2305, May/Jun. 2018, doi: 10.1109/TIA.2017.2787994.

[9] M. Tursini, E. Chiricozzi, and R. Petrella, “Feedforward flux-weakening control of surface-mounted permanent-magnet synchronous motors accounting for resistive voltage drop,” *IEEE Trans. Ind. Electron.*, vol. 57, no. 1, pp. 440–448, Jan. 2010.

[10] Y. Chen et al., “Improved flux-weakening control of IPMSMs based on torque feedforward technique,” *IEEE Trans. Power Electron.*, vol. 33, no. 12, pp. 10970–10978, Dec. 2018, doi: 10.1109/TPEL.2018.2810862.

[11] Y. Zhong, H. Lin, Z. Chen, S. Lyu, and H. Yang, “Online-parameter-estimation-based control strategy combining MTPA and flux-weakening for variable flux memory machines,” *IEEE Trans. Power Electron.*, vol. 37, no. 4, pp. 4080–4090, Apr. 2022, doi: 10.1109/TPEL.2021.3126581.

[12] S. Liu, C. Liu, H. Zhao, Y. Liu, and Z. Dong, "Improved flux weakening control strategy for five-phase PMSM considering harmonic voltage vectors," *IEEE Trans. Power Electron.*, vol. 37, no. 9, pp. 10967–10980, Sep. 2022, doi: 10.1109/TPEL.2022.3164047.

[13] Z. Zheng and D. Sun, "Model predictive flux control with cost function-based field weakening strategy for permanent magnet synchronous motor," *IEEE Trans. Power Electron.*, vol. 35, no. 2, pp. 2151–2159, Feb. 2020, doi: 10.1109/TPEL.2019.2921361.

[14] I. Gonzalez-Prieto, M. J. Duran, J. J. Aciego, C. Martin, and F. Barrero, "Model predictive control of six-phase induction motor drives using virtual voltage vectors," *IEEE Trans. Ind. Electron.*, vol. 65, no. 1, pp. 27–37, Jan. 2018, doi: 10.1109/TIE.2017.2714126.

[15] Y. Hu, Y. Li, X. Ma, X. Li, and S. Huang, "Flux-weakening control of dual three-phase PMSM based on vector space decomposition control," *IEEE Trans. Power Electron.*, vol. 36, no. 7, pp. 8428–8438, Jul. 2021, doi: 10.1109/TPEL.2020.3044574.

[16] S. Liu, C. Liu, Z. Song, Z. Dong, and Y. Huang, "Candidate modulation patterns solution for five-phase PMSM drive system," *IEEE Trans. Transp. Electrific.*, vol. 8, no. 1, pp. 1194–1208, Mar. 2022, doi: 10.1109/TTE.2021.3104876.

[17] S. Liu, Z. Song, Z. Dong, Y. Liu, and C. Liu, "Generic carrier-based PWM solution for series-end winding PMSM traction system with adaptative overmodulation scheme," *IEEE Trans. Transp. Electrific.*, early access, 2022, doi: 10.1109/TTE.2022.3193272.

[18] Y. Zhao and T. A. Lipo, "Space vector PWM control of dual three-phase induction machine using vector space decomposition," *IEEE Trans. Ind. Appl.*, vol. 31, no. 5, pp. 1100–1109, Sep./Oct. 1995, doi: 10.1109/28.464525.

[19] S. Liu, C. Liu, Y. Huang, and H. Zhao, "Model predictive two-target current control for OW-PMSM," *IEEE Trans. Power Electron.*, vol. 36, no. 3, pp. 3224–3235, Mar. 2021, doi: 10.1109/TPEL.2020.3016714.

[20] K. Yu, Z. Wang, X. Wang, and Z. Zou, "An online flux estimation for dual three-phase SPMSM drives using position-offset injection," *IEEE Trans. Power Electron.*, vol. 36, no. 10, pp. 11606–11617, Oct. 2021, doi: 10.1109/TPEL.2021.3067669.

[21] S. Liu, C. Liu, Y. Huang, and Y. Xiao, "Direct modulation pattern control for dual three-phase PMSM drive system," *IEEE Trans. Ind. Electron.*, vol. 69, no. 1, pp. 110–120, Jan. 2022, doi: 10.1109/TIE.2021.3053880.

[22] Y. Xu, B. Zheng, G. Wang, H. Yan, and J. Zou, "Current harmonic suppression in dual three-phase permanent magnet synchronous machine with extended state observer," *IEEE Trans. Power Electron.*, vol. 35, no. 11, pp. 12166–12180, Nov. 2020, doi: 10.1109/TPEL.2020.2989624.

[23] S. Liu and C. Liu, "Direct harmonic current control scheme for dual three-phase PMSM drive system," *IEEE Trans. Power Electron.*, vol. 36, no. 10, pp. 11647–11657, Oct. 2021, doi: 10.1109/TPEL.2021.3069862.

[24] S. Agoro and I. Husain, "Model-free predictive current and disturbance rejection control of dual three-phase PMSM drives using optimal virtual vector modulation," *IEEE J. Emerg. Sel. Topics Power Electron.*, early access, 2022, doi: 10.1109/JESTPE.2022.3171166.

[25] W. Taha, D. F. Valencia, Z. Zhang, B. Nahid-Mobarakeh, and A. Emadi, "Adaptive flux weakening controller for dual three-phase PMSM drives in vector space decomposition," in *Proc. 47th Annu. Conf. IEEE Ind. Electron. Soc.*, 2021, pp. 1–6.

[26] S. V. Nair, K. Layek, and K. Hatua, "An unequal split dual three-phase PMSM with extended torque-speed characteristics for automotive application," *IEEE Trans. Power Electron.*, vol. 37, no. 10, pp. 12437–12449, Oct. 2022.

Senyi Liu (Member, IEEE) received the B.Eng. and M.Eng. degrees in vehicle engineering from Tongji University, Shanghai, China, in 2015 and 2018, respectively, and the Ph.D. degree in electrical and electronic engineering from City University of Hong Kong (CityU), Hong Kong, in 2021.

He is currently a Postdoctoral Fellow with CityU. His main research interests include advanced control of motor drive systems, electric servo system, and wireless power transmission.

Zaixin Song (Member, IEEE) received the B.Eng. and M.Eng. degrees in electrical engineering and automation from the Harbin Institute of Technology, Harbin, China, in 2016 and 2018, respectively, and the Ph.D. degree in electrical engineering from City University of Hong Kong (CityU), Hong Kong, in 2021.

He is currently a Postdoctoral Research Fellow with CityU.

Dr. Song is currently the Chair Guest Editor of Special Issue in Energies, MDPI, and the Session Chair of 23rd IEEE International Conference on Industrial Technology 2022.

Yuxin Liu (Student Member, IEEE) received the B.Eng. degree in electrical engineering and automation from Tongji University, Shanghai, China, in 2017, and the M.Eng. degree in electrical engineering from the South China University of Technology, Guangzhou, China, in 2020. He is currently working toward the Ph.D. degree in electrical and electronic engineering with the City University of Hong Kong, Hong Kong.

His main research interests include power electronics, wireless power transmission, and control of power converters.

Yong Chen (Student Member, IEEE) received the B.Eng. and M.Eng. degrees in electrical engineering from Southeast University, Nanjing, China, in 2017 and 2020, respectively. He is currently working toward the Ph.D. degree in electrical and electronic engineering with the City University of Hong Kong, Hong Kong.

His main research interests include advanced control of motor drive systems and multimotor system.

Chunhua Liu (Senior Member, IEEE) received the B.Eng. and M.Eng. degrees in automatic control from the Beijing Institute of Technology, Beijing, China, in 2002 and 2005, respectively, and the Ph.D. degree in electrical and electronic engineering from The University of Hong Kong, Hong Kong, in 2009.

He is currently an Associate Professor in electrical and electronic engineering with the School of Energy and Environment, City University of Hong Kong, Hong Kong. His research interests include electric machines and drives, electric vehicles and aircrafts, electric robotics and ships, renewables and microgrids, power electronics, and wireless power transfer. In these areas, he has authored or coauthored more than 250 refereed papers. In addition, he is an RGC Research Fellow, Distinguish Lecturer of the IEEE Vehicular Technology Society, and World's Top 2% Scientists according to metrics compiled by Stanford University.

Dr. Liu is currently an Associate Editor for IEEE Transaction on Industrial Electronics, and an Editor for IEEE Transactions on Vehicular Technology, IEEE Transactions on Energy Conversion, and *IEEE Power Engineering Letters*. He is also an Editor for *Energies*, the Subject Editor for *IET – Renewable Power Generation*, an Associate Editor for *Open Journal of the Industrial Electronics Society*, an Associate Editor for IEEE Chinese Journal of Electrical Engineering, an Associate Editor for *CES Transactions on Electrical Machines and Systems*, an Associate Editor for *Elsevier Green Energy and Intelligent Transportation*, and an Editor for IEEE Transactions on Magnetics – Conference. In addition, he is the Chair and Founder of both Hong Kong Chapter, IEEE Vehicular Technology Society, and Hong Kong and Guangzhou Joint Chapter, and IEEE Industrial Electronics Society.